

Alloying Interlayers for Anode-Less Lithium-Metal Polymer Batteries

Michael J. Counihan, Dominik Steinle, Ritu Sahore, Katie Browning, Harry M. Meyer III, Annalena Krude, Lennart Wichmann, Gunther Brunklaus, Martin Winter, Andrew Westover, Dominic Bresser, and Sanja Tepavcevic*

Anode-less lithium-metal batteries potentially offer further increased energy densities. However, the Coulombic efficiency (CE) of lithium plating and stripping, as a classical measure of Li inventory reversibility, is commonly still insufficient for achieving long-lasting rechargeable batteries. Herein, the potential benefits of employing thin (20 nm) metal interlayers of Ag, Pt, and Au on Cu to alloy with Li in Cu||Li half-cells and induce homogeneous Li plating with poly(ethylene oxide)-based electrolytes are investigated. Interestingly, not all alloying interlayers enable a higher CE compared to neat Cu foil with 84%—specifically Ag@Cu with only 81%, while the best performing one, Au@Cu, provides a substantially increased CE of 91%. While generally the formation of “dead lithium” is found to be the major source of CE, this appears to be less pronounced in the case of Au@Cu, indeed. Further improvement can be achieved by carefully adjusting the cell voltage to a region in which the continuous de-/alloying is suppressed, yielding a further enhanced CE of 94%, thus highlighting the need for a comprehensive approach to design suitable electrode chemistries and designs beyond a “simple” material improvement.

Also termed “anode-free,” “Li free,” or “low N/P lithium metal,”^[2] these batteries require highly efficient lithium plating and stripping to sustain the battery over its lifetime due to the limited lithium inventory from the cathode.^[3,4] The Coulombic efficiency (CE) of the lithium plating and stripping process is dependent on the reactivity of Li metal with the electrolyte,^[5] the formation and stability of any solid-electrolyte interphase (SEI),^[6,7] and the morphology of the lithium^[8,9] plated on the current collector. All these aspects are related to each other and are determined by electrolyte chemistry,^[10] cell-level characteristics and engineering.^[11,12]

Using solid polymer electrolytes (SPEs) in anode-less SSLMBs offers potentially the highest energy density of all SSLMBs due to the inherent low density and the ease- of manufacturing low thickness of polymer layers relative to other solid electrolytes.^[13] Despite these benefits, our previous work demonstrated that with SPEs, the CE of Li plating and stripping is fundamentally limited with nickel and copper current collectors.^[14] Half cells using both commonly studied poly(ethylene oxide) (PEO) and novel single-ion conductor SPEs showed that Li metal CE was restricted to a maximum of 85%,

1. Introduction


Solid-state lithium metal batteries (SSLMBs) utilizing “anode-less” cell designs with no excess Li metal at the anode offer the highest energy density among current solid-state battery technologies.^[1]

previous work demonstrated that with SPEs, the CE of Li plating and stripping is fundamentally limited with nickel and copper current collectors.^[14] Half cells using both commonly studied poly(ethylene oxide) (PEO) and novel single-ion conductor SPEs showed that Li metal CE was restricted to a maximum of 85%,

M. J. Counihan, S. Tepavcevic
Materials Science Division
Argonne National Laboratory
Lemont, IL 60439, USA
E-mail: sanja@anl.gov

D. Steinle, D. Bresser
Helmholtz Institute Ulm (HIU)
89081 Ulm, Germany

D. Steinle, D. Bresser
Karlsruhe Institute of Technology (KIT)
76021 Karlsruhe, Germany

 The ORCID identification number(s) for the author(s) of this article can be found under <https://doi.org/10.1002/ssstr.202500429>.

© 2025 The Author(s). Small Structures published by Wiley-VCH GmbH. This is an open access article under the terms of the Creative Commons Attribution License, which permits use, distribution and reproduction in any medium, provided the original work is properly cited.

DOI: 10.1002/ssstr.202500429

R. Sahore, K. Browning, H. M. Meyer III, A. Westover
Chemical Sciences Division
Oak Ridge National Laboratory
Oak Ridge, Tennessee 37831, USA

A. Krude, L. Wichmann, G. Brunklaus, M. Winter
Forschungszentrum Jülich GmbH
Helmholtz-Institute Münster (IMD-4)
48149 Münster, Germany

M. Winter
MEET Battery Research Center
Institute of Physical Chemistry, University of Münster
48149 Münster, Germany

D. Bresser
Ulm University (UULm)
89069 Ulm, Germany

regardless of electrolyte chemistry, lithium reservoir amount, or cycling protocol. This limitation was partially assigned to dead lithium formation, where Li metal is left isolated from the current collector during plating or stripping processes.^[15,16] Dead Li formation is exacerbated by uneven nucleation and growth of Li metal leading to high surface area Li deposits, likely becoming electronically insulated from the current collector and impossibly being completely stripped.^[17,18]

A common approach in the anode-less SSLMB field is to use alloys of lithium with other metals to nucleate Li metal more homogeneously on the current collector.^[19–23] In particular, Ag has emerged as the best singular alloying metal due to its large capacity for Li, solid solution formation, and smooth transition to Li metal plating following saturation of the alloy.^[19,24] Virtually, all studies with this approach use hard inorganic solid electrolytes,^[21,25] but it is unknown if this approach is applicable to soft organic polymer electrolytes^[26] that are more similar to liquid electrolytes. The operating mechanism of these alloy-based electrodes in SSLMBs has been shown to be dependent on adhesion between the solid electrolyte, alloy layer, lithium metal, and current collector,^[22,27–29] something that will vary significantly between polymers and inorganic electrolytes.

Most of the works related to anode-free concepts are dealing with inorganic solid electrolytes.^[19,20,22] In this work, we merge the anode-free concept with organic polymer electrolytes, as there is a huge lack of available literature in this field (probably due to the fact of the very poor performance). This article does not aim to provide “breakthroughs” in terms of cyclability, CE, longevity etc. Here, we explore alloying metal interlayers in anode-less SSLMBs with PEO-based quasi-SPEs to determine which factors maximize CE of lithium plating and stripping. Ag, Pt, and Au thin films on Cu current collectors alloy with Li, followed by plating with lower overpotentials than Cu alone, although these interlayers also lose more Li inventory to electrochemical SEI formation. A new cycling protocol based on plated Li reservoirs is used to quantify CE of the Li_xM alloys and Li metal separately. Au@Cu electrodes (Cu foils sputtered with Au; see the experimental section) show the lowest long-term Li inventory losses and highest CE for both Li and total charge (see the later text for a complete description of the two types of efficiencies defined here), with CEs up to 91% and 95%, respectively. Ag@Cu electrodes performed worse than bare Cu electrodes over time ($\text{CE} < 80\%$), presumably due to the solubility of Ag into dead Li leading to rapid degradation of the interlayer. Prelithiation of Au@Cu reduced the initial SEI-related Li loss by 80% but worsened the overall CE, likely due to increased surface roughness and poor contact with the SPE, as revealed by XPS. Finally, controlling cell potential to prevent Li_xAu dealloying further increased the Li CE to 94% which is shown to be critical for long-term electrode stability. This work demonstrates for the first time a $>90\%$ lithium metal CE with quasi-SPEs and offers several routes to improve efficiency in anode-less SSLMBs.

2. Results and Discussion

2.1. Effect of Metal Chemistry on Lithium Plating

Numerous studies have used metals that alloy with lithium as anodes or as seed layers to enable lithium metal plating with

more even deposition than nonalloying current collectors.^[30,31] We systematically explored a similar approach with SPEs, where thin films (20 nm) of various alloying metals were sputtered onto copper foil current collectors. These M@Cu electrodes are combined with quasi-SPEs to obtain anode-less SSLMBs (**Figure 1a**). Since lithium alloys with late-transition and post-transition metals, Cu, Ag, Pt, and Au were chosen as alloying layers (**Figure 1b**). Since energy density is limited more at cell and pack level, negative impact of thin alloy layers on energy density is negligible. Based on rough calculations for a cylindrical “Samsung INR21700-50 E 5000 mAh 10–15 A Li-Ion” battery module, it turned out that considering a thin metal layer of 100 nm will increase the entire weight of this battery of only around 250 mg in the case of Au and Pt and only around 130 mg in the case of Ag. However, especially in the case of gold, the high gold price would lead to additional material costs of more than 26 US\$ for such a battery. (For silver only about 16 ct!). For solid-state batteries in particular, Ag has emerged as the best candidate due to its unparalleled capability to uptake Li to form the alloy ($x = 1\text{--}12+$ in Li_xAg),^[32,33] with Au also showing promise ($x = 0.17\text{--}3+$ in Li_xAu).^[25,31,34,35] Pt should be similar to Au in many regard ($x = 0.14\text{--}2+$ in Li_xPt).^[36] Cu served as the base current collector and also served as the control case, as little to no alloying ($x < 0.01$ in Li_xCu) occurs at room temperature.^[37,38]

To study how each metal thin film affects lithium plating, 20 nm of Ag, Au, or Pt were sputtered onto pretreated Cu electrodes. M@CuLi half cells were prepared with SPEs consisting of 70 wt% PEO and 30 wt% tetraglyme with LiTFSI in a 10:1 EO:Li molar ratio (70-30 PEO-TEGDME) and galvanostatically cycled at 40 °C. **Figure 2a** shows the initial charging step from representative cells at a low current density of $20 \mu\text{A cm}^{-2}$. Prior to lithium deposition at voltages $< 0\text{V}$, initial SEI formation (2.0–0.0 V) and alloy formation of the different metals (below 0.3 V) takes

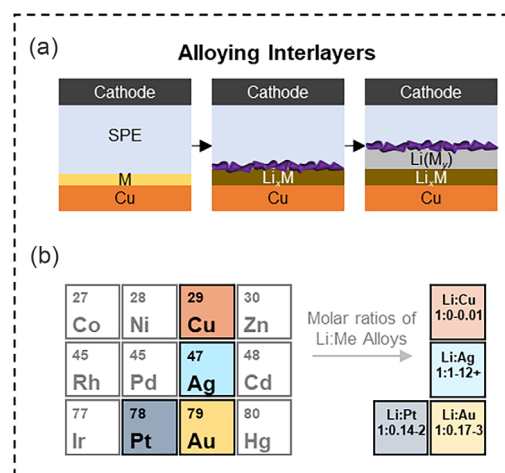


Figure 1. a) Schematic of alloying interlayers in SPE-based batteries. Charging of the cell leads to SEI formation (purple) and metal alloying (Li_xM) positive of 0.0 V vs. $\text{Li}^{0/+}$. Once the metal is completely alloyed or the cell voltage exceeds the thermodynamic potential for Li plating, Li metal plates on the alloyed Li_xM layer. Small amounts of the metal may be soluble in the Li phase as Li(M) . b) Transition metals chosen for this study and the range of Li_xM molar ratios in experimentally known alloy phases.

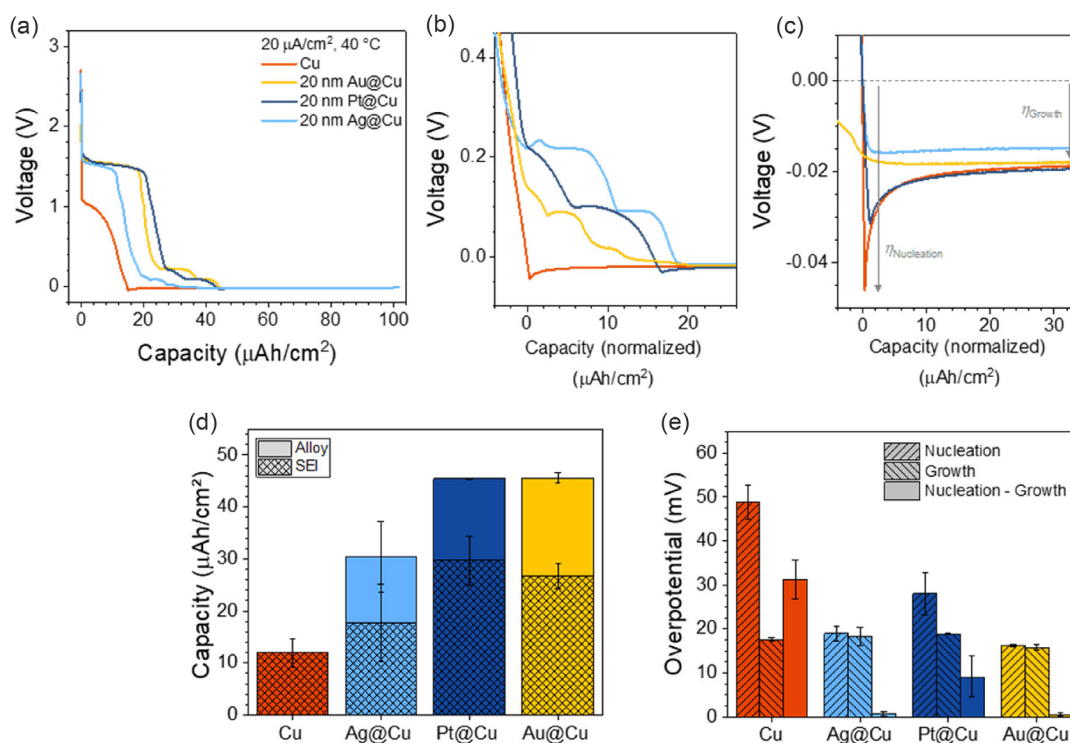


Figure 2. a) First $100 \mu\text{Ah cm}^{-2}$ charging step in M@CuLi half cells. b) Detailed view of the voltage profiles, where the x-axis capacity is shifted with respect to post-SEI formation for better comparison of the samples. c) Detailed view of the voltage profiles in the Li plating regime, where the x-axis capacity is shifted with respect to the capacity accumulated after 0.0 V vs. Li^0 . d) Estimated capacity from initial SEI formation and from the alloying steps in the first charging step from (a) and (b). e) Estimated nucleation, growth, and nucleation-minus-growth overpotentials from (c). Values and error bars are averages and standard deviations from 2-3 individual cells (see according plating profiles in Supporting Information S1, Figure S1).

place (in parallel). Figure 2b plots these alloying steps adjusted and normalized with respect to the alloying onset. Ag@Cu, Pt@Cu, and Au@Cu electrodes show distinct plateaus relating to their different alloy compositions before the onset of lithium plating below 0.0 V. Figure 2c shows this lithium plating onset region in more detail, again adjusted with respect to the Li-plating onset for comparison between electrode types. Cu electrodes display a clear peak then decline to steady voltage associated with Li nucleation and growth regimes, respectively. Analogous processes can be observed for Pt@Cu electrodes, but with a reduced overpotential for nucleation. While Ag@Cu electrodes exhibit a very small and broad nucleation region; a smooth transition from alloying into Li growth is observed for Au@Cu electrodes.

All of these processes have important implications for lithium charge and energy efficiency, rendering it important to quantify their contributions to efficiency losses in the cell. As discussed above, the initial conditioning of the anode-free cells (prior to lithium plating below 0 V) includes a contribution from electrolyte decomposition (initial SEI formation) and a contribution from alloying reactions. The initial SEI formation leads to an irreversible loss of lithium inventory. Figure 2d shows that Cu electrodes exhibited the lowest capacity loss to initial SEI formation ($12 \pm 3 \mu\text{Ah cm}^{-2}$). All metal films increased the capacity consumed during initial SEI formation especially with Pt ($30 \pm 5 \mu\text{Ah cm}^{-2}$) and Au ($27 \pm 2 \mu\text{Ah cm}^{-2}$) thin films. The greater overall lithium loss may be due to a higher surface

area of the sputtered electrodes, but the initial SEI formation may also be catalyzed by these heavier transition metals, as evidenced by both the greater SEI-formation capacities and higher reduction potentials compared to Cu.

Second, the amount of lithium used for alloying the thin film also reduces the lithium inventory, depending on how reversible the (de-)alloying process is (vide infra). Figure 2d shows that the capacity of alloy formation to be less than $20 \mu\text{Ah cm}^{-2}$ with each 20 nm metal layer which is both less than the initial SEI-formation capacity and negligible in the context of SSB target capacities of $\geq 3 \text{ mAh cm}^{-2}$.^[39] Independent of how much Li goes into the alloy phase, film thickness will control anode's gravimetric capacity depending on the density of the metal film. For example, to maintain the target value of 3000 mAh g^{-1} total of anode capacity, thin films should not exceed thicknesses of: 100 nm for Pt, 110 nm for Au, and 210 nm for Ag. Figure S2 in the Supporting Information S2 shows how metal film thickness impacts with regard to specific capacity of the anode side. The alloyed capacities correspond to Li:M molar ratios of 2.4:1 Li:Ag, 2.7 Li:Pt, and 3.6 Li:Au. It is very likely that some amount of initial SEI formation occurred simultaneously with alloying in this first charge step, making these Li:M values higher than the actual alloy composition. Nevertheless, the trend of Au alloying more than Pt aligns with the expected Li_xM phases (Figure 1b). For Ag, it is likely that alloying continued below the 0.0 V threshold, but this is difficult to quantify.

Third, the overpotentials related to lithium metal plating are indicative of the Li plating process and determine the energy efficiency of the battery. Figure 2e shows the nucleation and growth overpotentials for the different electrode types, as well as the difference between these values, as defined in Figure 2c. Nucleation overpotentials followed $\text{Au@Cu} \leq \text{Ag@Cu} < \text{Pt@Cu} < \text{Cu}$, with Au@Cu being one third of the bare Cu value. This shows that alloyed Li_xM layers make it easier to nucleate Li metal, as demonstrated previously in liquid and other solid electrolytes,^[20,31] but the improvement is dependent on the alloying chemistry. In contrast, growth overpotentials are essentially the same in all cases, with only minor differences between electrodes in the 16–19 mV range. This indicates that there is little difference for growing Li on Li already formed on $\text{Li}_x\text{M@Cu}$ or Cu and that there are minimal increased surface area effects for the alloy thin films (as higher surface areas would lower growth overpotentials). The difference between nucleation and growth demonstrates how much the alloy layer lowers the barrier for Li nucleation onto non-Li metal compared to continued plating on Li metal. For Cu and to a lesser extent Pt@Cu, these values are significant (31 and 9 mV, respectively), indicating the base (alloyed) electrode is not conducive to Li nucleation. For Ag@Cu and Au@Cu, these values are essentially 0 mV, showing that the high levels of lithiation caused a smooth transition from nucleation to plating, seen qualitatively in Figure 2c. For Ag, this has been shown to result from Li metal phase separation out of over-lithiated Li_xAg phases;^[32,33] a similar process may happen for Li_xAu alloys. The nonzero nucleation-minus-growth overpotential of Pt@Cu indicates that i) the Pt is not completely alloyed to its maximum extent and so cannot achieve the same trends as Ag@Cu and Au@Cu, and/or ii) the alloyed Li_xPt phase (presumably Li_2Pt) is not of sufficient lithium content or surface energy^[40] to create a barrier-free transition from Li nucleation to growth.

2.2. CE of Anode Processes

Reversibility of charge and discharge processes determines the capacity fade in a battery and is often assessed by the CE. Given the limited capacity reservoir in anode-less batteries, the CE at the Li metal electrode determines their longevity. In the simple case, this CE gives reflects of how much Li can be stripped in relation to the amount that was plated. For electrodes with alloying interlayers, CE is a more complicated calculation due to the different distributions of (ir)reversible Li inventory in the Li_xM and Li phases as well as the irreversible SEI formation. To separate the effects of initial SEI formation, reversibility of alloying, and Li plating/stripping, we used a modified galvanostatic cycling protocol based on the reservoir (also known as Aurbach or Adams) method.^[41,42] As shown in **Figure 3a**, a M@Cu||Li half-cell was charged initially with a current density of $20 \mu\text{A cm}^{-2}$ and areal capacity of $100 \mu\text{Ah cm}^{-2}$ to form the initial SEI, alloy the interlayer, and plate some amount of Li to “precondition” the electrode. The cell was then discharged to 0.10 V, where only Li metal should be stripped, but the alloy should mostly remain intact (since all metals used here nearly do not de-alloy lithium until positive of 0.10 V).^[20,21] This initial plate/strip cycle comprised the so-called “precondition step.” A reservoir of lithium with a capacity of $100 \mu\text{Ah cm}^{-2}$ was then

plated onto the preconditioned electrode surface (stripped but still-alloyed). Next, a 20% fraction of the reservoir capacity ($20 \mu\text{Ah cm}^{-2}$) was stripped and plated repeatedly for 9 cycles, followed by a complete discharge to 0.5 V with a constant voltage hold at 0.5 V to strip all Li and dealloy M@Cu . All these steps were performed with the same current density of $20 \mu\text{A cm}^{-2}$.

Using this method, we quantified four distinct Coulombic efficiencies (see equations in Figure 3a), each providing unique information to facilitate understanding and comparisons of Li inventory loss mechanisms across the four metal substrates.

1. Initial CE (CE_{Init}): CE of the initial preconditioning cycle; this informs about Li inventory loss from SEI formation and alloying during the first battery plating step.

$$CE_{\text{Init}} = \frac{Q_{\text{S}}^{\text{Init}}}{Q_{\text{SEI}} + Q_{\text{Alloy,Ch}} + Q_{\text{P}}^{\text{Init}}} \quad (1)$$

2. Alloy and initial SEI CE ($CE_{\text{Alloy+SEI}}$): A ratio of dealloying capacity during the final stripping step relative to the sum of initial alloying and SEI formation capacities; this informs about Li inventory loss from non-Li metal processes.

$$CE_{\text{Alloy+SEI}} = \frac{Q_{\text{Alloy,Dis}}}{Q_{\text{SEI}} + Q_{\text{Alloy,Ch}}} \quad (2)$$

3. Total reservoir CE ($CE_{\text{Total}}^{\text{Res}}$): CE of the total stripping capacity relative to the total plating capacity in the protocol (excluding the 1st preconditioning cycle); this informs about the total Li loss over an extended period of cycling after the preconditioning step.

$$CE_{\text{Total}}^{\text{Res}} = \frac{Q_{\text{S}}^{\text{Res}} + Q_{\text{Alloy,Dis}} + n(0.2 \times Q_{\text{P}}^{\text{Res}})}{Q_{\text{P}}^{\text{Res}} + n(0.2 \times Q_{\text{P}}^{\text{Res}})} \quad (3)$$

4. Lithium-only reservoir CE ($CE_{\text{Li}}^{\text{Res}}$): same as the *Total Reservoir CE* except for exclusion of the final dealloying capacity from the calculations; this informs about the efficiency of Li plating/stripping onto the Li_xM alloy obtained after the preconditioning step.

$$CE_{\text{Li}}^{\text{Res}} = \frac{Q_{\text{S}}^{\text{Res}} + n(0.2 \times Q_{\text{P}}^{\text{Res}})}{Q_{\text{P}}^{\text{Res}} + n(0.2 \times Q_{\text{P}}^{\text{Res}})} \quad (4)$$

Separating CE values in this manner should provide insight into how the different metal chemistries influence not only Li plating and stripping but total Li inventory loss in the cell over time. The above cycling protocol was repeated five times for a given cell, with altered current densities and/or the number of short strip/plate cycles in the middle, to evaluate its long-term Li inventory loss under varying cycling conditions (complete details in the Supporting Information S3-1). The sequential repetitions of the protocol are referred to as “rounds,” and the results are shown in Figure 3b,d and Figure S33a,3b, Supporting Information. The maximum current density of the polymer electrolyte used herein was measured by linear sweep voltammetry and ranges around $500 \mu\text{A cm}^{-2}$. However, dendrite formation was observed in this current regime. To exclude effects accompanied by dendrites, we selected a maximum current of $100 \mu\text{A cm}^{-2}$ being far below this value.

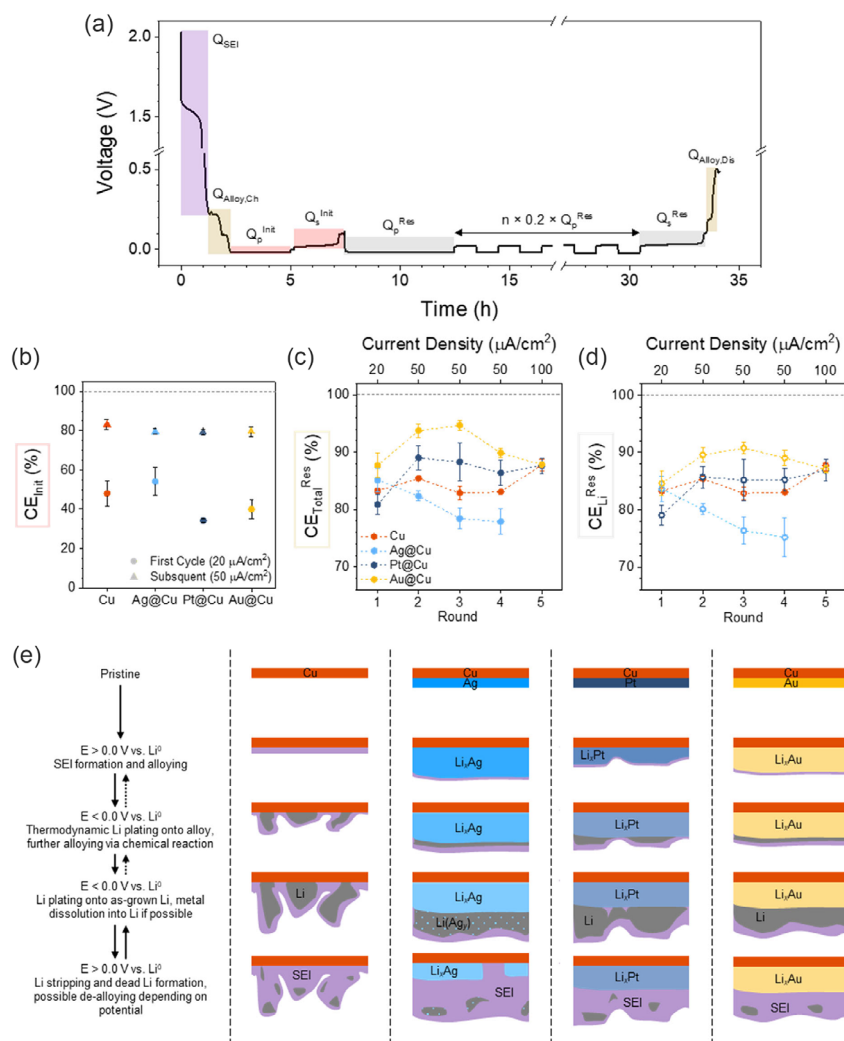


Figure 3. a) Example voltage profile of the modified reservoir method cycling protocol. Relevant quantities to calculate Coulombic efficiencies are given on the graph. b) Initial CE from the first 20 $\mu A/cm^2$ charge step and a subsequent step at 50 $\mu A/cm^2$ for each electrode type. c) Total Reservoir CE (CE_{Total}^{Res}) and d) Lithium-only Reservoir CE (CE_{Li}^{Res}) values from the reservoir steps for each electrode type at different current densities over the cell lifetime. e) Proposed mechanisms explaining overpotential and CE trends for each electrode type.

Figure 3b shows CE_{Init} (CE of the precondition step) for the different electrode types obtained during the 1st round at 20 $\mu A/cm^2$ (right after cell assembly) and during the 2nd round at 50 $\mu A/cm^2$. In the 1st round, Cu and Ag@Cu outperformed Pt@Cu and Au@Cu due to the lower amount of initial SEI formation (Figure 2a). Since the SEI is already formed during the 1st precondition cycle and the alloy layers are completely dealloyed after the 1st round by stripping by going to 0.5 V cut-off, the Li loss during 2nd round's preconditioning step would only be from the realloying process which was determined to be similar for all three interlayers. Indeed, all electrodes behaved similarly in the 2nd round. Interestingly, for Cu, where no alloying reactions are present, CE_{Init} of the 2nd round still only reached 80%, suggesting either breakage of existing SEI or new Li nuclei formation on top of the existing SEI. These results show that preventing Li loss in the very first plating step is an important way to keep Li inventory, something which will be addressed later below.

In contrast, long-term cycling (five rounds of the Figure 3a cycling protocol in sequence with slight protocol modifications each time) revealed important CE trends. Figure 3c,d, show CE_{Total}^{Res} and CE_{Li}^{Res} (see Figure 3a equations) obtained for each electrode type during the five rounds, respectively. Round 1 was a 20 $\mu A/cm^2$, rounds 2–4 were at 50 $\mu A/cm^2$, and round 5 was at 100 $\mu A/cm^2$. In the first round, both the CE types followed the $Au@Cu > Ag@Cu > Cu > Pt@Cu$ trend with values of 81–88% for CE_{Total}^{Res} and 79–85% for CE_{Li}^{Res} . At higher current densities and longer timescales (rounds 2–4), however, different trends emerged. Au@Cu electrodes still outperformed every other electrode type, achieving up to 95% CE_{Total}^{Res} and 91% and CE_{Li}^{Res} at 50 $\mu A/cm^2$. Pt@Cu slightly outperformed Cu with both CE_{Total}^{Res} and CE_{Li}^{Res} values in the 80–89% range, but both the CE values dropped continuously for Ag@Cu the longer the cell was cycled, eventually dropping below 80%. Despite the similarities in preconditioning CE (CE_{Init}) and alloying overpotentials

between Ag and Au, some distinct chemical difference that leads to this dramatic drop-off in efficiency (vide infra) during long-term cycling, as discussed later. Interestingly, at the highest current density of $100 \mu\text{A cm}^{-2}$, no difference was observed between Cu, Pt@Cu, and Au@Cu (all CEs $\approx 87\%$), with very little capacity contribution from the alloying/dealloying process compared to at 20 and $50 \mu\text{A cm}^{-2}$. This indicates that the nucleation benefits from M@Cu layers disappear at high currents and supports the usage of low current densities in this study ($20, 50 \mu\text{A cm}^{-2}$) to evaluate the different alloying behaviors of the various metallic interlayers and their evolution with slow long-term cycling. While these low currents are impractical for commercial applications, this study can help guide the choice of an ideal interlayer that could induce homogenous Li nucleation during a slower cell formation cycle. For the sake of a clearer overview of the experiment's results, the maximum values of the different CEies (from Figure 3) as well as the values from Figure 2 are summarized in the Table S3-2 of Supporting Information S3-2.

For a deeper analysis of this experiment, the total capacity losses and loss rates of each cell from Figure 3 were calculated and plotted in the Supporting Information S3-3, Figure S3-3, to demonstrate how Ag@Cu performed compared to other alloying interlayers. A brief discussion is also included there.

Despite the initial electrochemical similarities of these metal interlayers (initial SEI formation/alloying capacities and overpotentials), their differing mechanisms behind alloying and lithium plating likely led to these differences in efficiency. Based on the above-discussed results, the mechanisms behind these differences are hypothesized in Figure 3e. In the first step, electrodes are biased to just above 0.0 V vs. Li^0 , leading to initial SEI formation on all electrodes and alloying in the case of Ag@Cu, Pt@Cu, and Au@Cu. Ag and Au alloy with Li to higher stoichiometries ($x > 2$ in Li_xM), while Pt is only alloying up to a maximum of Li_2Pt . These differences in Li uptake are leading to differences in surface lithiophilicity finally resulting in differences of Li nucleation in the second step: Cu nucleates unevenly, $\text{Li}_x\text{Pt@Cu}$ nucleates slightly better but not completely homogeneously, while $\text{Li}_x\text{Ag@Cu}$ and $\text{Li}_x\text{Au@Cu}$ are able to nucleate Li with near uniformity. In the third step, Li growing on the nucleated Li is expected to retain some amount of the initial Li layers' characteristics, i.e., heterogeneous Li nuclei will grow high surface area Li deposits while the even Li layers will grow more compact, low surface area layers. In the fourth step, stripping the grown Li leads to dead Li formation, which is exacerbated with high surface area Li and leads to lower CE. Since Au@Cu forms the best Li nuclei, it shows the highest CE values and lowest rate of charge loss.

In the case of Ag@Cu, Ag will dissolve to a small extent into the Li metal phase^[20,33] because of its high solubility in Li (Figure 1b). In principle, this is a benefit as Ag allows for high Li capacity uptake, potentially making it very attractive for high energy density battery designs.^[32,33] However, this is problematic for solid electrolyte system forming an (initial) SEI which is not capable to prevent dead Li formation. As Li is deposited, the alloyed layer might leach Ag into all of the connected Li deposits as $\text{Li}(\text{Ag}_y)$. Upon stripping, as dead $\text{Li}(\text{Ag}_y)$ is continuously formed, it eventually depletes the alloying layer. After enough plating-stripping cycles, Ag@Cu electrodes essentially resemble Cu electrodes but with sparse Ag remaining on the electrode and dead $\text{Li}(\text{Ag}_y)$ deposits near the electrode surface. This apparently leads to even lower

CE than Cu electrodes (Figure 3c,d) due to even more heterogeneous growth on the Ag@Cu and bare Cu areas and/or Li growth in the presence of the dead $\text{Li}(\text{Ag}_y)$ layer, which increases the interface resistance considerably.^[16] It is also noteworthy that in the case of silver (in opposite to Au case) a slight dissolution of Ag (0.5 at%) into lithium lead to a relatively severe reduction of its lattice parameter potentially causing mechanical failure/delamination of the alloy layer contributing to the poor performance of Ag.^[32] Since Au is not known to notably dissolve into Li,^[34] Au@Cu electrodes maintain their high performance, at least in the timescales tested here (several days). It was found that the initial alloying reaction is not following the formation of thermodynamically stable alpha and beta phases according to phase diagram but instead led to the formation of a phase similar to delta and then followed by AuLi_3 and, in some conditions, $\text{Au}_4\text{Li}_{15}$. These phases seem to reversibly (re-)form during (de-)alloying. However, a hysteresis is observed in the low lithium content regime during further delithiation (dealloying) process, presumably revealing the alpha and beta phases.^[35] The occurrence of these low-lithium containing alpha- and beta phases during the dealloying process might account for a more controlled delithiation process and somehow support the conservation the Au layer's "architecture" of the gold layer leading to less amount of unconnected ("dead") Li (with Au dissolved). For these alloying interlayers to be practically useful, Ag@Cu electrodes that show similar lower overpotentials to Au@Cu—but importantly have ≈ 80 times lower material cost^[44]—must be paired with engineered electrolytes and electrode-electrolyte interphases to eliminate dead Li formation and eventually loss of the Ag layer. This experimental concept can in principle be transferred to any other (polymer-) electrolyte as well as liquid electrolytes since the manufacturing process of the thin-film alloying anodes is universal.^[14,44]

2.3. Effect of Alloy Prelithiation

Au@Cu achieved over 90% CE for Li plating and stripping in the above-discussed results (Figure 3), well above other values reported for these types of SPEs (50–80%).^[14] Still, the gap between 90% and 99.9+ % is large and must be overcome to enable batteries 100+ cycle lifetimes.^[45] To increase the lithium inventory and, hopefully improve the CE, we prelithiated Au@Cu electrodes by depositing 100 or 200 nm Li metal via thermal evaporation prior to cell assembly (Figure 4a). In contact with the SPEs during cell assembly, these should chemically form the SEI and potentially leave behind a Li_xAu layer. Therefore, the presence of a chemically preformed SEI layer along with some level of Li in the Li_xAu layer prior to cycling should reduce the first cycle lithium inventory loss observed with M@Cu electrodes (Figure 2a,d).

Figure 4b shows the first charge steps for half cells with Au@Cu, 100 nm Li@Au@Cu, and 200 nm Li@Au@Cu electrodes (the Au thickness in all cases was 20 nm). A vast majority of the electrochemical SEI formation was negated due to chemical SEI formation from the Li@Au@Cu electrodes. Surprisingly, there was little change in the alloying behavior (Figure 4c), indicating that virtually all of the Li in both 100 and 200 nm Li@Au@Cu films was consumed by side reactions, which is also apparent based on the open circuit potentials of the cells being

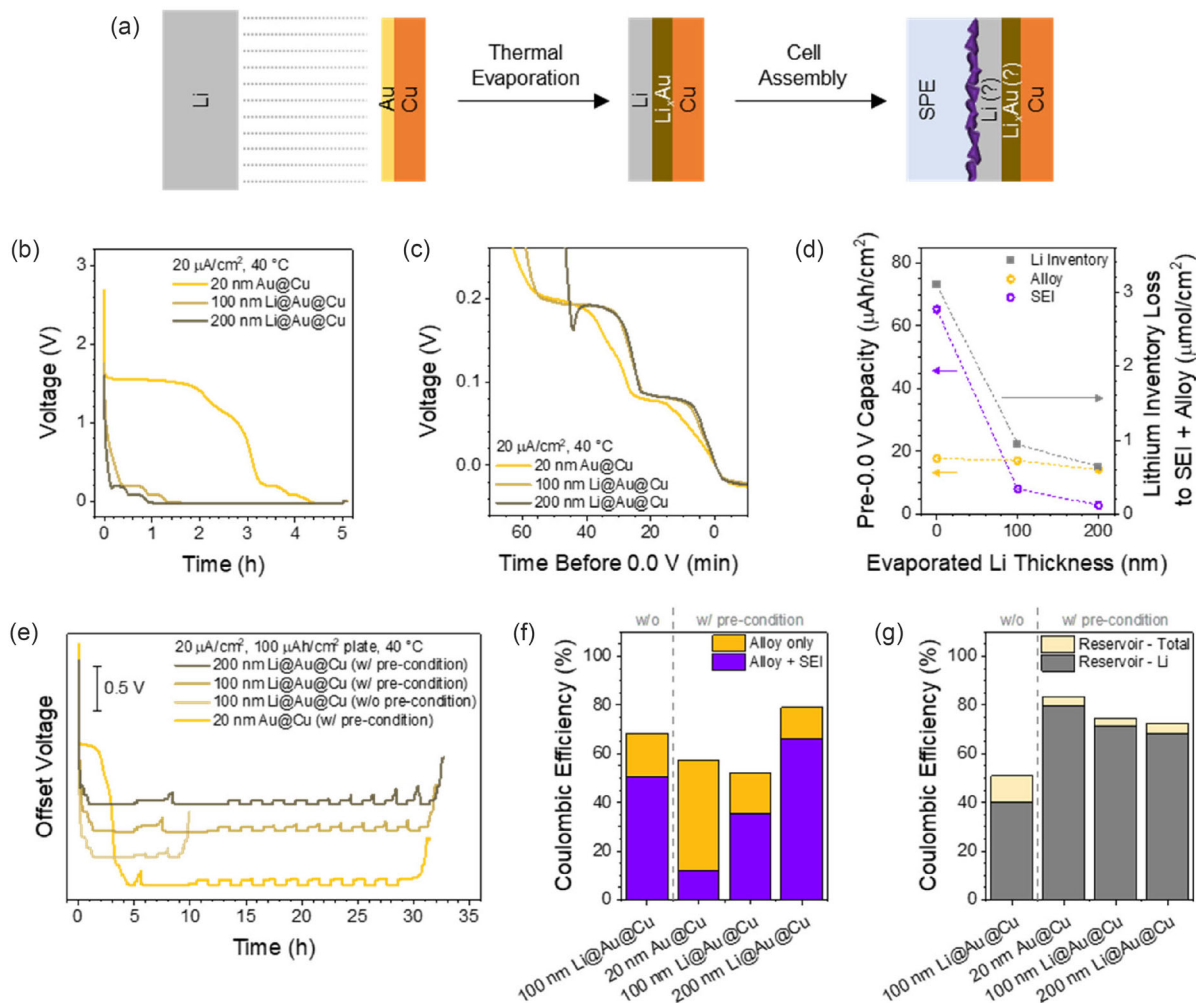


Figure 4. a) Schematic of the Au@Cu prelithiation and cell fabrication process. b) First 100 $\mu\text{Ah cm}^{-2}$ charge step in 20 nm Au@Cu/Li half cells with 0, 100, and 200 nm Li prelithiation amounts. c) Comparison of the Au alloying region from voltage profiles in (b), where the x-axis time is charging time before 0.0 V vs. Li^0 . d) Estimated charge loss from SEI and alloy formation from (b) and the total lithium inventory loss from these steps. e) Cycling profiles for cells with 0, 100, and 200 nm Li prelithiation amounts; “precondition” refers to the preconditioning steps in Figure 3. f) CE of the cells related to the alloy + SEI capacities ($\text{CE}_{\text{Alloy}+\text{SEI}}$) and alloy capacity alone. g) Total Reservoir CE ($\text{CE}_{\text{Total}}^{\text{Res}}$) and Li-only Reservoir CE ($\text{CE}_{\text{Li}}^{\text{Res}}$) values for each cell.

well above the potentials of Li_xAu phases ($>1\text{ V}$ instead of $\leq 0.3\text{ V}$). This led to significant Li inventory savings from SEI formation but not from the alloying, as quantified in Figure 4d. Still, the total Li inventory loss from these two steps was reduced by 80% for 200 nm Li@Au@Cu compared to pristine Au@Cu. X-ray photoelectron spectroscopy (XPS) depth profiling of as-made 100 and 200 nm Li@Au@Cu films indicated that all of the excess deposited Li (more than what would be needed for a 100% alloying), as well as some of the Li in the prelithiated Li_xAu films underneath was already consumed by the trace moisture and CO_2 in the argon glovebox atmosphere in which the thermal evaporation was performed, to form $\text{LiOH}/\text{Li}_2\text{CO}_3/\text{Li}_2\text{O}$ (Figures S4-1, 3, Supporting Information).

Despite the Li inventory saving from the presence of a pre-formed SEI, these electrodes did not show the improvements in the cells’ overall reversibility, when cycled similar to Figure 3a protocol (Figure 4e). Au@Cu showed the highest CE with no Li

depletion occurring before the final step in the reservoir protocol. For both 100 and 200 nm Li@Au@Cu, the Li reservoir seems to have depleted within the first six to eight strip-plate steps. For 100 nm Li@Au@Cu cycled without the preconditioning step prior to reservoir cycling, the CE is exceptionally poor, with depletion after two steps. The Coulombic efficiencies for various processes with these electrodes are plotted in Figure 4f,g. Prelithiated electrodes do show higher CE for alloy+SEI processes (see Figure 3a, for $\text{CE}_{\text{Alloy}+\text{SEI}}$ equation) compared to pristine Au@Cu, and generally higher alloy CEs (the latter can be extracted by use of the equation for $\text{CE}_{\text{Alloy}+\text{SEI}}$ just without the SEI capacity contribution Q_{SEI}). However, for Li plating and stripping, Au@Cu still had the highest CE values for both the Total Reservoir CE ($\text{CE}_{\text{Total}}^{\text{Res}}$) and Li-only Reservoir CE ($\text{CE}_{\text{Li}}^{\text{Res}}$), the only sample to achieve over 80% CE in this set of tests.

The reasons for the lack of improvement in lithium-cycling CEs could be numerous and interconnected. First, the

uniformity of the Li layers is crucial to ensure homogeneous plating, but XPS measurements and scanning electron microscopy (SEM) imaging of the as made prelithiated films show that the Au seed layer gets significantly roughened after prelithiation. (see Figures S4-1–S4-3, Supporting Information, and the associated discussion). Second, SEI characteristics are likely different between the two cases. For the case of Au@Cu electrode, SEI was electrochemically formed and therefore the SEI species will have SPE's compositional signature. However, as mentioned above, a native passive film composed of LiOH/Li₂CO₃/Li₂O had already formed at the surface of as-made Li@Au@Cu films from exposure to trace moisture and CO₂ in the argon glovebox atmosphere. Since the SEI composition is known to control dead Li formation, this could heavily influence CE values.^[10,15] Third, the electrochemomechanics of the alloyed layers (ex-situ vs. in-situ) may be different. More detailed studies are required to decouple the impacts of roughness, SEI chemistry, and alloying-electrochemomechanics, on the C.E. This will be explored in-depth in a separate study. Here, we aimed to present a first-order investigation of prelithiation as one of the strategies to improve the baseline C.E. values (Figure 3).

2.4. Cell Voltage Limits

After optimizing the metal interlayer chemistry and observing no improvements in Li CE via prelithiation, we finally sought to improve CE by adjusting electrochemical cell parameters, specifically, the cut-off voltage for the Li stripping process. In the previous experiments, Au@Cu electrodes were discharged to 0.5 V, which ensured a complete dealloying of the Li_xAu phases. Therefore, we investigated the effect of varying the cut-off potential to control the degree of dealloying and its impact on CE. Here, CE was calculated conventionally as the ratio of discharge capacity to charge capacity.

The cut-off voltage for the discharge of CuLi and Au@CuLi half cells was varied between 0.1 and 0.8 V during repeated plating and stripping at 50 and 100 $\mu\text{Ah cm}^{-2}$ capacity (Figure 5a). For CuLi case, higher cut-off voltages generally led to higher discharge capacities in the initial stages (Figure 5b (top)). A similar trend was observed for Au@CuLi, though not immediately obvious, as the discharge capacity for the 0.4 V cut-off case is slightly higher than for 0.8 V. This anomaly is explained when the differences in ratios of initial Li plating capacities vs. alloying

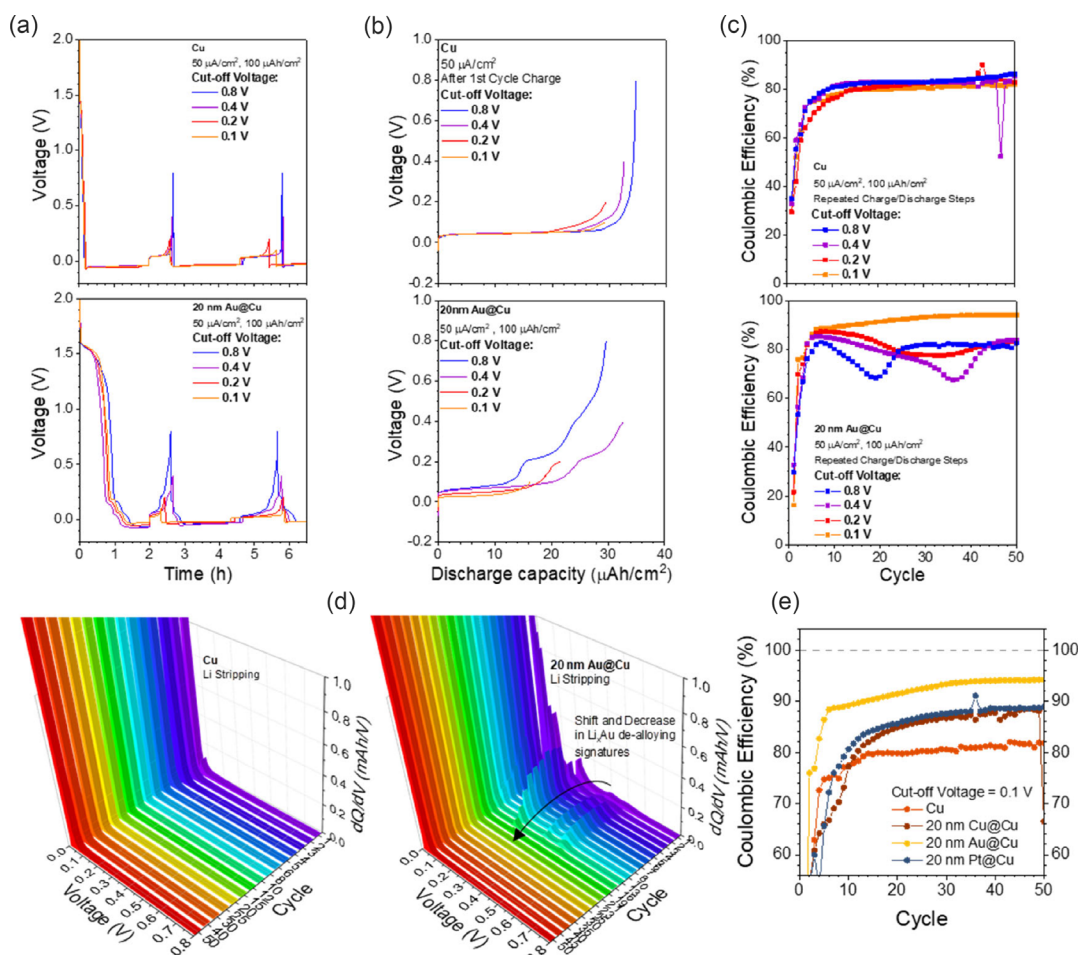


Figure 5. a) Example voltage profiles of the first two charge-discharge steps for CuLi (top) and 20 nm Au@CuLi (bottom) half cells at 40 °C, where the discharge step is ended at different cell voltages. b) Comparison of usable capacity from the first discharge steps in (a). c) Individual cycle CEies for CuLi (top) and 20 nm Au@CuLi (bottom) cells with various cut-off voltages. d) Differential capacity curves from select cycles of CuLi (left) and 20 nm Au@CuLi cells (right) with 0.8 V cut-off voltages. e) Individual cycle CEies for M@CuLi half cells with 0.1 V cut-off voltages.

capacities (charge) are considered for these cells (see Figure 5a (bottom)). Since neat Li plating/stripping capacity (not alloying/dealloying) contributed significantly to total charge/discharge capacity for these cells, the effect of a lower degree of dealloying got suppressed for the case of 0.4 V cut-off. With this in mind, in general, the increase of cut-off voltage is accompanied by increasing the discharge capacity but goes at the cost of depleting Li in the Au interlayer. The CE for individual cycles of Cu and Au@Cu cells are shown in Figure 5c. For bare Cu, there is little difference in CE for cells discharged to 0.1 or 0.8 V (all CE values 80–85% after 50 cycles). However, for Au@Cu, the differences are obvious and clearly show the effects of alloy depletion. For cut-off voltages that fully deplete the alloy (0.4–0.8 V), a decrease in the CE followed by increase is detected at earlier times with higher voltages, i.e., more aggressive dealloying. This is evident in differential capacity (dQ/dV) curves over the cell lifetime (Figure 5d), where a shift and decrease in dQ/dV peaks (at around 0.2 V) indicate progressive dealloying of the Li_2Au phase. The degradation of Li_xAu alloy layers may be due to mechanisms similar to Ag@Cu electrodes in Figure 3c, where small amounts of Au solubilize into or attach to Li and are lost as dead Li(Au), or due to delamination of the film from repeated expansion and contraction during alloying and dealloying. Given the shift in cell lifetime at which CE decreases with varying cut-off voltages (Figure 5c, bottom), it seems likely that the delamination mechanism dominates here.

The highest CE values are achieved with Au@Cu electrodes at a 0.1 V cut-off voltage, reaching over 90% after 14 cycles and 94% after 40 cycles, in agreement with results from reservoir method cycling protocols in Figure 3. This voltage limit prevents dealloying of the Li_xAu layer, avoiding the sudden CE decrease observed at higher voltage cut-offs (Figure 5c, bottom). Aside from stability of the Li_xAu layer, higher CE could be attributed to accumulation of residual Li left behind from incomplete stripping in the previous cycles. However, this is not observed for the Cu electrode at a 0.1 V cut-off voltage, where CE values 12% lower than Au@Cu. Additionally, higher surface area from the sputtered metal layer could lead to lower local current density and thus reduce the chance for dead Li formation. Figure 5e shows that sputtering nonalloying Cu onto Cu (20 nm Cu@Cu) slightly improves the CE from 82% to 88% at 50 cycles, but these changes are not more than Pt@Cu and remain lower than Au@Cu, indicating that surface area effects are marginal. These two observations demonstrate that preservation of the Li_xAu alloyed seed layer by controlling the cell potential is the main reason behind improved Li plating-stripping CE in the long-term.^[46]

3. Conclusions

We have shown that thin layers of metals alloying with lithium metal can improve the CE of Li metal anodes with quasi-SPEs. Ag, Pt, and Au on Cu current collectors all lower the nucleation overpotential for Li plating, with Ag and Au reducing it to essentially 0 mV. These metal interlayers increase the charge loss to electrochemical initial SEI formation to three times relative to bare Cu electrodes. After the initial formation cycle, CE follows the trend $\text{Au@Cu} > \text{Pt@Cu} \geq \text{Cu} > \text{Ag@Cu}$ for both total charge efficiency and Li plating-stripping efficiency. Au@Cu

electrodes achieve up to 95% total CE and 91% Li CE at $50 \mu\text{A cm}^{-2}$ current densities and have the lowest rate of Capacity loss among all tested electrodes. The mechanisms behind these trends are proposed and hypothesized, wherein Ag@Cu electrodes fail rapidly due to the solubility of Ag in Li metal and subsequent loss through dead Li formation. Prelithiation of Au@Cu electrodes via thermal evaporation of Li metal decreases Li inventory losses by up to 80% by eliminating electrochemical SEI formation, but the CEs with prelithiated electrodes are lower than pristine Au@Cu, possibly due to the chemomechanics of the (de-)alloyed interlayers. Finally, Li plating-stripping efficiency is increased to 94% with Au@Cu electrodes when the cell voltage is controlled to strip only to 0.1 V vs. Li^0 , which preserves the Li_xAu alloy layer for homogeneous Li deposition in subsequent cycles. This is the first demonstration to our knowledge of reaching >90% CE at the lithium metal anode with quasi-SPEs. However, the obtained fundamental findings of CuLi half-cells herein and the underlying mechanisms of Li inventory losses can provide a valuable toolbox for the design of application oriented full cell systems. Combining this alloying interlayer approach with optimized PE chemistries and interface engineering could allow for anode-less battery systems with >99% CE, closer approaching the target of real battery applications. In our future work on the anode-free concept coupled with organic electrolytes, we will continue to address challenges related to interfacial issues. Apart from chemical modification (e.g., incorporation of additives) to account for deficits in terms of ionic conductivity and interfacial problems, bridging the gap for the achievement of higher CEies, engineering efforts for appropriate current collector design might be also considered allowing organic electrolytes to be successfully applied in anode-free cell configurations.

4. Experimental Section

Materials: PEO (−4 Mio g/mol), lithium bis(trifluoromethanesulfonyl) imide (LiTFSI, >99.5%), tetraethyleneglycol dimethylether (TEGDME, 99%), and benzophenone (BP, 99%) were purchased from Union Carbide, 3M, Acros Organics, and Merck, respectively. Copper foil (6 and 40 μm thickness, 99.8%) was purchased from MSE Supplies and VWR. Cu, Ag, Pt, and Au sputter targets were acquired from Lesker with at least 99.99% metal purity.

SPE Preparation: SPEs were prepared similarly to previous reports^[14,47] by mixing PEO and TEGDME in weight ratios of 70:30 or 50:50 along with LiTFSI to yield a mixture with $\text{EO:Li} = 10:1$ mol:mol. BP was added for a weight fraction of 5% photo initiator. This mixture was mixed in a glass vial by spatula sealed under vacuum in pouch bag foil and heated at 100 °C for 12 h. The gummy mixture was then pressed between two Mylar sheets at 20 bar and 100 °C and exposed to UV light in a UV curing chamber from Hönle equipped with a Fe irradiation source with an intensity of 10 W cm^{-2} for 3 min each side. The membrane thickness was typically 70 μm . All preparations were performed in a dry room (dew point < −70 °C).

Electrode Preparation: Cu electrodes were prepared by punching Cu foil discs of 1.0 cm^2 area. The discs were briefly soaked in 1 M H_2SO_4 before rinsing with MilliQ water followed by acetone to remove the native oxide layer. The electrodes were then dried under vacuum at 60 °C before use. For Ag@Cu, Pt@Cu, and Au@Cu electrodes, pretreated Cu electrodes were transferred to a high vacuum sputter system (element Pi) before sputtering with the target metal at deposition rate of $1.0 \pm 0.1 \text{ Å s}^{-1}$ to the desired thickness of 20 nm. Sputtered electrodes were also dried at 60 °C under vacuum before transfer to the glovebox.

Electrochemical Measurements: Half cells were tested with M@Cu working electrodes and Li foil (MTI, 250 μm thick) counter electrodes. The electrode areas were 0.9–1.1 cm^2 . SPEs were sandwiched between both electrodes before assembly into coin cells with 1.0 mm stainless steel spacer and wave spring (for reservoir method cycling experiments) or pouch cells with nickel tabs (for cut-off voltage and NMR experiments) inside Ar-filled gloveboxes. The applied pressure in both cases is less than 0.3 MPa. Cells were cycled at 40 $^\circ\text{C}$ after equilibrating the temperature for several hours. Full cells utilizing lithium iron phosphate (LFP) composite cathodes were prepared similarly with 2.09 mgLFP cm^{-2} loadings on Al foil manufactured at the Cell Analysis, Modeling, and Prototyping (CAMP) Facility at Argonne National Laboratory.

Lithium Evaporation: Thermal evaporation of lithium metal was performed with a custom-built Kurt J. Lesker vacuum system with base pressures around 5×10^{-8} Torr, from a Ta crucible using a rate-controlled method. Au-coated Cu foil discs (1/2" diameter) were loaded into the chamber, and Li was deposited at a rate of 40–60 \AA s^{-1} . Nominal Li thicknesses of 100 and 200 nm were deposited on the Au@Cu electrodes, which were stored in a glovebox (Ar/ CO_2 mixed atmosphere) prior to use.^[48]

Materials Characterization: XPS: The as-made prelithiated Li@Au@Cu electrodes (100 nm Li@Au@Cu and 200 nm Li@Au@Cu) samples were mounted for analysis in an Ar-filled glovebox using the vacuum transfer module (VTM) for the K-Alpha XPS instrument. After inserting the samples into the XPS instrument through a vacuum-pumped load-lock, an initial wide energy range survey spectrum was acquired to determine all elements present. Next, a set of narrow energy range core level spectra were acquired for each identified element. An Ar-ion depth profile was then done on each sample to follow the film composition as a function of sputter time, which can be estimated as depth. Depth profiles were done by alternately acquiring data for the elements of interest (C, O, Au, Li, and Cu) and then sputtering for 15 s. Plotting the composition as a function of sputter time yielded the depth profiles. In separate experiments, 100 nm thick SiO_2 films were etched to determine a sputter rate. If the Au-Li films sputter at the same rate as SiO_2 , then the sputter rate can be used to convert sputter time to depth. For SiO_2 , the measured sputter rate was 12 nm min^{-1} . At the end of the depth profile, survey and core level data were acquired on the well-sputtered surface. The B.E.s were aligned w.r.t the C 1s peak at 284.8 eV. After the depth profiles, the Au 4f was used for alignment at 84.0 eV when no carbon was present.

Materials Characterization: SEM: SEM was performed on the surface of Cu foil, as-made Au@Cu foil, and as-made prelithiated 100 nm Li@Au@Cu foil. To ensure an air-free transfer of the prelithiated sample into an SEM, an in-house-built SEM sample transfer holder was used, in which the samples are sealed with vacuum, before transferring the sealed-holder itself into the SEM chamber. The SEM sample transfer holder's design and operation were discussed previously by Howe et al.^[49] SEM images were collected by using a Zeiss Merlin FE-SEM microscope. The accelerating voltage used was 3 kV for the 100 nm Li@Au@Cu sample, and 10 kV for the bare Cu foil and Au@Cu samples. Post-processing the images included altering the brightness and contrast using the Microsoft PowerPoint's "Correction" feature to maximize the visibility of the various structural features within an image.

Supporting Information

Supporting Information is available from the Wiley Online Library or from the author.

Acknowledgements

[EERE, Tien, LISI] [Argonne – Steve Trask, CAMP facility] This work was supported by the Assistant Secretary for Energy Efficiency and Renewable Energy, Office of Vehicle Technologies of the U.S. Department of Energy, under contract no. DE-AC02-06CH11357 under the Advanced Battery Materials Research (BMR) and US-German Collaborative Research

Program. The LFP cathodes used in this work were produced by Steve Trusk at Argonne National Laboratory's Cell Analysis, Modeling, and Prototyping (CAMP) Facility, which is supported by the U.S. Department of Energy's Vehicle Technologies Office (VTO). Financial support by the Federal Ministry of Education and Research (BMBF, Germany) within the projects LISI2 (03XP0224E). [ORNL] The SEM in this work was performed and supported at the Center for Nanophase Materials Sciences in Oak Ridge National Lab, a DOE Office of Science user facility. The authors gratefully acknowledge the financial support by the German Federal Ministry of Education and Research (BMBF) within the project "LISI-2" (13XP0509A and 03XP0509D).

Conflict of Interest

The authors declare no conflict of interest.

Author Contributions

Michael J. Coughlan: conceptualization (equal); data curation (equal); formal analysis (equal); investigation (lead); writing—original draft (lead). **Dominik Steinhilber:** data curation (equal); formal analysis (equal); investigation (supporting); writing—original draft (supporting); writing—review and editing (supporting). **Ritu Sahore:** data curation (supporting); formal analysis (supporting); investigation (supporting); writing—original draft (supporting). **Katie Browning:** formal analysis (supporting); investigation (supporting). **Harry M. Meyer III:** data curation (supporting); investigation (supporting). **Annalena Krude:** conceptualization (supporting); investigation (supporting); methodology (supporting). **Lennart Wichmann:** investigation (supporting); methodology (supporting). **Gunther Brunklaus:** data curation (supporting); formal analysis (supporting); funding acquisition (supporting); project administration (supporting); supervision (supporting). **Martin Winter:** funding acquisition (supporting); methodology (supporting); project administration (supporting); resources (supporting); supervision (supporting). **Andrew Westover:** formal analysis (supporting); funding acquisition (supporting); investigation (supporting); methodology (supporting); project administration (supporting); supervision (supporting). **Dominic Bresser:** conceptualization (supporting); formal analysis (supporting); funding acquisition (supporting); methodology (supporting); project administration (supporting); resources (supporting); supervision (supporting). **Sanja Tepavcevic:** conceptualization (lead); formal analysis (equal); funding acquisition (lead); supervision (lead); writing—review and editing (lead).

Data Availability Statement

The data that support the findings of this study are available from the corresponding author upon reasonable request.

Keywords

anode-less battery, coulombic efficiency, dead lithium, lithium-alloying interlayer, polymer electrolyte

Received: June 29, 2025

Revised: August 18, 2025

Published online:

- [1] C.-H. Jo, K.-S. Sohn, S.-T. Myung, *Energy Storage Mater.* **2023**, 57, 471.
- [2] K. B. Hatzell, *ACS Energy Lett.* **2023**, 8, 4775.
- [3] D. Wang, J. Qiu, N. Inui, R. Hagiwara, J. Hwang, K. Matsumoto, *ACS Energy Lett.* **2023**, 8, 5248.

- [4] C. Zor, S. J. Turrell, M. S. Uyanik, S. Afyon, *Adv. Energy Sustain. Res.* **2024**, 5, 1.
- [5] T. Hasegawa, D. Mori, S. Taminato, Y. Takeda, O. Yamamoto, N. Imanishi, *ChemElectroChem* **2023**, 10, 1.
- [6] G. M. Hobold, C. Wang, K. Steinberg, Y. Li, B. M. Gallant, *Nat. Energy* **2024**, 9, 580.
- [7] Y. He, W. Fan, Y. Zhang, Z. Wang, X. Li, Z. Liu, Z. Lü, *ACS Appl. Mater. Interfaces* **2020**, 12, 22268.
- [8] L. Su, H. Charalambous, Z. Cui, A. Manthiram, *Energy Environ. Sci.* **2022**, 15, 843.
- [9] F. Ding, W. Xu, X. Chen, J. Zhang, M. H. Engelhard, Y. Zhang, B. R. Johnson, J. V. Crum, T. A. Blake, X. Liu, J.-G. Zhang, *J. Electrochem. Soc.* **2013**, 160, A1894.
- [10] G. M. Hobold, J. Lopez, R. Guo, N. Minafra, A. Banerjee, Y. S. Meng, Y. Shao-Horn, B. M. Gallant, *Nat. Energy* **2021**, 6, 951.
- [11] M. Genovese, A. J. Louli, R. Weber, S. Hames, J. R. Dahn, *J. Electrochem. Soc.* **2018**, 165, A3321.
- [12] K. L. Bassett, K. A. Small, D. M. Long, L. C. Merrill, B. Warren, K. L. Harrison, *Front. Batter. Electrochem.* **2023**, 2, 1.
- [13] Z. Song, F. Chen, M. Martinez-Ibanez, W. Feng, M. Forsyth, Z. Zhou, M. Armand, H. Zhang, *Nat. Commun.* **2023**, 14, 4884.
- [14] R. Sahore, A. Mayer, D. Steinle, M. J. Counihan, X. C. Chen, S. Tepavcevic, D. Bresser, A. S. Westover, *J. Electrochem. Soc.* **2024**, 171, 050505.
- [15] X.-R. Chen, C. Yan, J.-F. Ding, H.-J. Peng, Q. Zhang, *J. Energy Chem.* **2021**, 62, 289.
- [16] K. H. Chen, K. N. Wood, E. Kazyak, W. S. LePage, A. L. Davis, A. J. Sanchez, N. P. Dasgupta, *J. Mater. Chem. A* **2017**, 5, 11671.
- [17] D. Tewari, S. P. Rangarajan, P. B. Balbuena, Y. Barsukov, P. P. Mukherjee, *J. Phys. Chem. C* **2020**, 124, 6502.
- [18] R. Zhang, X. Shen, Y. Zhang, X. Zhong, H. Ju, T. Huang, X. Chen, J. Zhang, J. Huang, *J. Energy Chem.* **2022**, 71, 29.
- [19] Y.-G. Lee, F. Satoshi, J. Changhoon, S. Naoki, Y. Nobuyoshi, O. Ryo, D.-S. Ko, S. Tomoyuki, S. Toshinori, R. Saebom, *Nat. Energy* **2020**, 5, 299.
- [20] S. E. Sandoval, J. A. Lewis, B. S. Vishnugopi, D. L. Nelson, M. M. Schneider, F. J. Q. Cortes, C. M. Matthews, J. Watt, M. Tian, P. Shevchenko, P. P. Mukherjee, M. T. McDowell, *Joule* **2023**, 7, 2054.
- [21] W. J. Jeong, C. Wang, S. G. Yoon, Y. Liu, T. Chen, M. T. McDowell, *ACS Energy Lett.* **2024**, 9, 2554.
- [22] J. A. Lewis, K. A. Cavallaro, Y. Liu, M. T. McDowell, *Joule* **2022**, 6, 1418.
- [23] W. Jia, J. Zhang, L. Zheng, H. Zhou, W. Zou, L. Wang, *eScience* **2024**, 4, 100266.
- [24] Y. Ye, H. Xie, Y. Yang, Y. Xie, Y. Lu, J. Wang, X. Kong, S. Jin, H. Ji, *J. Am. Chem. Soc.* **2023**, 145, 24775.
- [25] C. Haslam, J. Sakamoto, *J. Electrochem. Soc.* **2023**, 170, 040524.
- [26] L. Bertoli, S. Bloch, E. Andersson, L. Magagnin, D. Brandell, J. Mindemark, *Electrochim. Acta* **2023**, 464, 142874.
- [27] Y. F. Gao, M. Cho, M. Zhou, *J. Mech. Sci. Technol.* **2013**, 27, 1205.
- [28] V. Mahajani, N. Koratkar, *Small* **2023**, 2306388, 1.
- [29] J. Li, H. Su, Y. Liu, Y. Zhong, X. Wang, J. Tu, *Electrochem. Energy Rev.* **2024**, 7, 18.
- [30] X. Gu, J. Dong, C. Lai, *Eng. Rep.* **2021**, 3, 1.
- [31] K. Yan, H. W. Lee, F. Xiong, P. C. Hsu, Y. Li, J. Zhao, S. Chu, Y. Cui, *Nat. Energy* **2016**, 1, 16010.
- [32] A. D. Pelton, *Bull. Alloy Phase Diagrams* **1986**, 7, 223.
- [33] S. Jin, Y. Ye, Y. Niu, Y. Xu, H. Jin, J. Wang, Z. Sun, A. Cao, X. Wu, Y. Luo, H. Ji, L. Wan, *J. Am. Chem. Soc.* **2020**, 142, 8818.
- [34] A. D. Pelton, *Bull. Alloy Phase Diagrams* **1986**, 7, 228.
- [35] S. Hejazi, R. Liang, A. Sergeenko, M. D. Fleischauer, *J. Electrochem. Soc.* **2024**, 171, 050518.
- [36] J. Sangster, A. D. Pelton, *J. Phase Equilibria* **1991**, 12, 678.
- [37] A. D. Pelton, *Bull. Alloy Phase Diagrams* **1986**, 7, 142.
- [38] R. Rupp, B. Caerts, A. Vantomme, J. Fransaer, A. Vlad, *J. Phys. Chem. Lett.* **2019**, 10, 5206.
- [39] Y. Lu, C. Z. Zhao, H. Yuan, J. K. Hu, J. Q. Huang, Q. Zhang, *Matter* **2022**, 5, 876.
- [40] M. Morey, G. Nagaro, A. Halder, S. Sharifzadeh, E. Ryan, *J. Energy Storage* **2024**, 92, 112144.
- [41] A. Mohammadi, S. Djafer, S. Sayegh, A. J. Naylor, M. Bechelany, R. Younezi, L. Monconduit, L. Stievano, *Chem. Mater.* **2023**, 35, 2381.
- [42] B. D. Adams, J. Zheng, X. Ren, W. Xu, J. Zhang, *Adv. Energy Mater.* **2018**, 8, 1.
- [43] Kitco Metals Inc., Precious Metals, <https://www.kitco.com/price/precious-metals>, (accessed: March 2025).
- [44] J. Oh, J. Kim, S. Bae, H. Kim, T. Lee, S. H. Choi, G. Park, S. Ji, K. J. Kim, J. W. Choi, *Adv. Energy Mater.* **2025**, 02711, 1.
- [45] J. Xiao, Q. Li, Y. Bi, M. Cai, B. Dunn, T. Glossmann, J. Liu, T. Osaka, R. Sugiura, B. Wu, J. Yang, J. G. Zhang, M. S. Whittingham, *Nat. Energy* **2020**, 5, 561.
- [46] Y. Xiao, R. Xu, L. Xu, Y. X. Zhan, J. F. Ding, S. Zhang, Z. H. Li, C. Yan, J. Q. Huang, *Adv. Energy Mater.* **2023**, 13, 1.
- [47] K. Geng, T. Eisenmann, R. Parmar, J. Rezvani, R. Gunella, M. Amati, L. Gregoratti, D. Stepien, T. Diemant, D. Bresser, *J. Electrochem. Soc.* **2022**, 169, 110521.
- [48] A. S. Ho, A. S. Westover, K. Browning, J. A. Maslyn, D. Y. Parkinson, R. Sahore, N. Dudley, N. P. Balsara, *ACS Energy Lett.* **2022**, 7, 1120.
- [49] J. Y. Howe, L. A. Boatner, J. A. Kolopus, L. R. Walker, C. Liang, N. Dudley, C. R. Schaich, *J. Mater. Sci.* **2012**, 47, 1572.